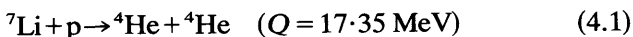


# 4

## Some apparatus of nuclear physics

In 1932 Cockcroft and Walton succeeded in producing artificial transmutation by accelerated ions. They observed the (p,  $\alpha$ ) process



using protons of energy 100–500 keV. Since their work, the technology of accelerators has developed extensively and much of our knowledge of nuclear structure and reactions derives from experiments using accelerated ions and electrons. Only in neutron physics does another type of radiation source, the nuclear reactor, provide comparable amounts of information.

Despite the fact that several fundamental particles were discovered in cosmic radiation (Ch. 2), the properties of particles and resonances have been established in the main by accelerator experiments. Beyond the limit of accelerator energies, cosmic rays have regained their original role as a source of new information.

The requirements of an accelerator for nuclear structure studies are, broadly speaking, an energy sufficient to overcome the Coulomb repulsion between the accelerated ion and its target nucleus and a resolution and an energy variability capable of responding to details of the nuclear-level spectrum. The Coulomb barrier height for the uranium nucleus is approximately 15 MeV for an incident proton and the precision of nuclear reaction data is now often better than  $\pm 1$  keV. The electrostatic generator, the cyclotron and the linear accelerator have all been developed to meet the specification in whole or in part. In particle physics, centre-of-mass energy, coupled with reasonable intensity, is still a paramount obligation. The requirement is best met by the proton or electron synchrotron or the electron linear accelerator, although if intensity can be sacrificed a related storage-ring system provides a very large increase in available energy.

Detecting systems have similarly evolved to meet specific requirements and to match accelerator performance. In nuclear structure studies, energy-loss and full energy signals from solid-state detectors provide particle identification and energy measurement for light

charged particles with a line width of  $<10$  keV at 30 MeV, for instance. The fabrication of large semiconductor detectors has permitted line widths of about 1 keV to be reached in the determination of photon energies. Visual methods of detection, having almost vanished from low-energy experiments, have assumed a vital role in particle physics, above all in cases in which the maximum information associated with an interaction vertex is required. Most neutrino experiments could hardly be conceived without the bubble or spark chamber. Hybrid systems combining electronic triggers with large-aperture detectors are providing increased data rates. Position-sensitive detectors are used in both high- and low-energy physics to read events in the focal plane of spectrometers or to indicate particle trajectories.

Vital ancillaries to the accelerator-detector systems are the beam transport and data acquisition systems, which are themselves large and complex installations, designed always to increase the effectiveness of overall performance.

Finally, mention should be made of the energies lying between those of particle physics and of nuclear structure, the intermediate energy range from, say, 100 MeV to 2000 MeV. This is the domain of the high-energy probes of nuclear structure throwing light on short-range correlations between nucleons and has produced its own special group of accelerators, within which are found the so-called 'meson-factories'.

References 4.1–4.4 cover the material of this chapter, and much more, in depth.

#### 4.1 The tandem electrostatic generator (Ref. 4.1)

Cockcroft and Walton employed a transformer-rectifier-condenser voltage multiplying unit to accelerate protons to a velocity  $v$  given by

$$\frac{1}{2}m_p v^2 = eV \quad (4.2)$$

where  $V$  is the output voltage of the generator on load. Generation of a voltage up to about 5 MV by cascade multiplying circuits operating at high frequencies and enclosed in pressure vessels is still an important technique when high-intensity beams of both protons and electrons are required. For general nuclear structure research, however, by far the most versatile and powerful accelerator is the electrostatic generator developed by Van de Graaff in 1931.

This generator is a direct illustration of the definition of the potential of a conductor as the work done in bringing unit charge from a standard reference point to the conductor. In the electrostatic generator the conductor forms the high-potential terminal of an evacuated accelerating tube (Fig. 4.1, lower half) in which ions of

the required type move, emerging with a high velocity at the earth potential end of the tube. Charge is conveyed to the terminal by an endless insulating belt, or in recent systems by a series of conductors insulated from each other but forming a flexible chain. Transfer of charge is made to the belt or chain at the low-potential end by a corona discharge from spray points, as indicated in Fig. 4.1 (or by electrostatic induction in the case of a chain). At the terminal end the transfer process is reversed, and by allowing the terminal pulley to reach a higher potential than the terminal itself, negative charge may be conveyed to the downgoing belt. In one large modern installation it is planned to deliver a charging current of up to 550  $\mu\text{A}$  to the terminal; this has to supply not only the accelerated beam current but also all losses due to corona discharges and leakage through the insulators forming the 'stack' structure necessary to support the accelerating tube and terminal. The stack structure itself is essentially a series of equipotential surfaces separated by rigid insulators and connected by resistors. Its electrical function is to provide a uniform axial electric field, within which the accelerator tube is contained, and which avoids regions of high field strength that may lead to breakdown.

Electrostatic generators are normally enclosed in a pressure vessel filled with an insulating gas, to permit the terminal voltage to be raised to a level corresponding to an overall axial voltage gradient of about  $2 \text{ MV m}^{-1}$ , which can be withheld by a long accelerating tube. This is generally the weakest part of the electrical structure, and to attain the necessary gradient magnetic suppression of secondary electrons produced within the tube may be necessary.

The radial voltage gradient at the terminal for cylindrical geometry is given by the formula

$$E_r = V/(r \ln (R/r)) \quad (4.3)$$

where  $V$  is the potential of the central terminal,  $r$  its radius and  $R$  the inner radius of the pressure vessel. For a given  $E_r$  (of perhaps  $20 \text{ MV m}^{-1}$ , determined by breakdown in the insulating gas),  $V$  is a maximum when  $R/r = e$ . The most effective insulating gas is sulphur hexafluoride ( $\text{SF}_6$ ) and pressures of up to 100 atmospheres are used in large machines.

In the early electrostatic accelerators ions were injected into the accelerating tube from a gaseous discharge tube housed in the terminal. However, in the *tandem* accelerator, shown in Fig. 4.1, the ion source is at earth potential and produces negative ions, e.g.  $\text{H}^-$ ,  $\text{He}^-$ ,  $^{16}\text{O}^-$ . These are accelerated to the terminal through an extension of the accelerating tube already mentioned. In the terminal,  $\text{H}^-$  ions, for instance, are moving with a velocity  $v$  given by (4.2) and passage through a thin *stripper*, e.g. a carbon foil of thickness about  $50 \mu\text{g cm}^{-2}$  or a tube containing gas at low pressure, removes the

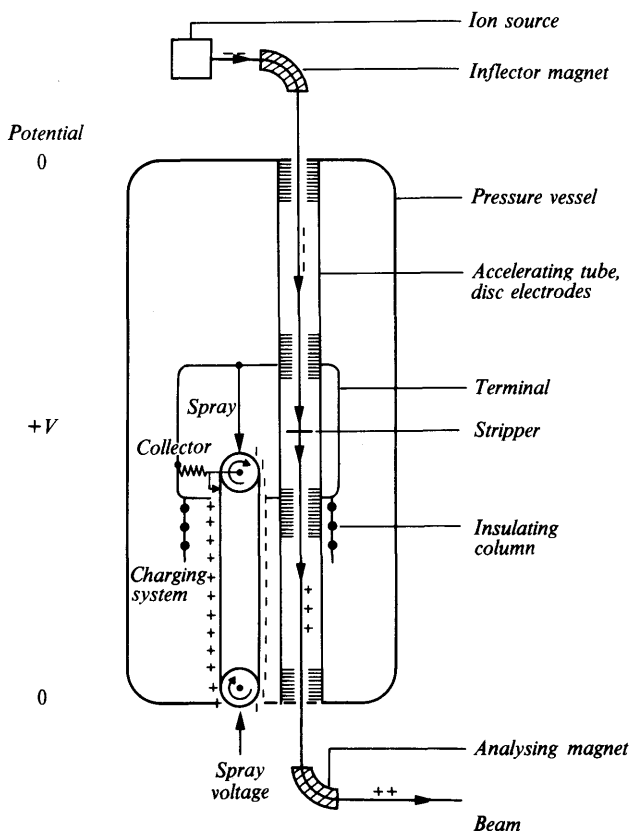


Fig. 4.1 The electrostatic generator (schematic). The lower half is effectively a single-ended machine and the addition of the upper half with an extra tube and a stripper converts it to a tandem accelerator.

extra electron and a further electron as well so that a positive ion  $H^+$  is available for acceleration to earth potential from the terminal, yielding an energy of  $2\text{ eV}$ . Negative ions of heavier elements may be stripped to a positive charge state  $qe$  in the terminal and the final velocity in this case corresponds to acceleration through a potential  $(1+q)V$ ; additional strippers in the positive-ion tube can be used to increase  $q$ .

The energy of an electrostatic generator may be stabilized by controlling the charging current from an error signal derived from the accelerated beam itself. This passes through an analysing magnet (Fig. 4.1) and an exit slit with insulated jaws, from which a difference signal is derived if the beam deviates from the axis.

Energy definition to about  $0.5\text{ keV}$  is possible in this way with a spread about the mean energy of not more than  $1\text{--}1.5\text{ keV}$  even in

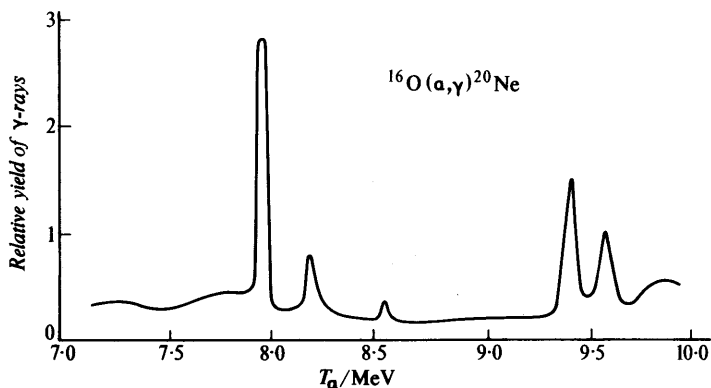


Fig. 4.2 Yield of capture gamma rays in the reaction  $^{16}\text{O}(\alpha, \gamma)^{20}\text{Ne}$  as a function of incident  $\alpha$ -particle energy (Pearson, J. D. and Spear, R. H., *Nuclear Physics*, **54**, 434, 1964).

the largest accelerators of, say, 20 MV terminal voltage supplying proton currents of say,  $10\ \mu\text{A}$ . This type of performance is ideal for nuclear reaction experiments. Figure 4.2 is a yield curve displaying nuclear resonances obtained in the  $^{16}\text{O}(\alpha, \gamma)$  reaction.

The tandem generator has the obvious advantage of easy access to its ion source, which can be a complex, multipurpose installation at ground potential. A further advantage, shared with other direct-current machines, is its continuous output, which is convenient for coincidence counting. For some experiments, however, timing is important and in the determination of reaction neutron energies by time-of-flight methods a pulsed beam may be obtained by deflecting the continuous beam at a frequency of about 5 MHz backwards and forwards across a narrow slit near the ion source. Further compression, to pulse widths of about 2 ns, may be obtained by velocity modulation (bunching) techniques.

The energy of the proton beam from a tandem accelerator operating in the 10–25 MeV range has been determined with a precision of 1 part in  $10^5$  by a time-of-flight method. The beam is passed through two radiofrequency deflectors separated by an accurately measured distance of about 150 m and it is arranged that a detector signal is obtained only when the time of flight corresponds with a precisely determined number of radiofrequency periods plus a known phase displacement.

## 4.2 Linear accelerators (Refs. 4.2 and 4.3)

It was early recognized that the extension of direct-voltage methods to the production of very high particle energies would ultimately

encounter insulation problems. The possibility of successive re-application of the same moderate electric field to a particle beam was, therefore, studied, and led to the development of the linear accelerator.

### 4.2.1 Drift-tube accelerators

The earliest heavy-particle accelerators (Wideroe 1928, Sloan and Lawrence 1931, Beams and Snoddy 1934) were of this type. The principle is illustrated in Fig. 4.3. In the Sloan–Lawrence accelerator, operated at approximately 30 MHz, a number of field-free drift tubes of length  $L_1, L_2, \dots, L_n$ , separated by small accelerating gaps, were connected alternately to the output terminals of an oscillator of free-space wavelength  $\lambda$ . The length of the drift tubes is such that the field in a gap just reverses in the time that a particle takes to pass from one gap to the next. If the voltage across each gap at the time of passage of the particles is  $V$  then the particle energy at entry to the drift tube numbered  $n$  (Fig. 4.3) is  $neV$  (for

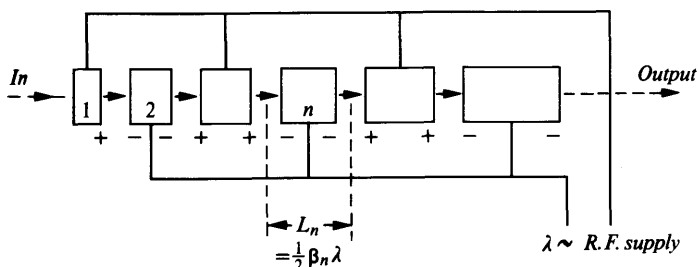


Fig. 4.3 Principle of the Sloan–Lawrence linear accelerator.

an assumed initial injection energy of  $eV$ ) and the particle velocity is

$$v_n = (2neV/M)^{1/2} \quad (4.4)$$

where  $M$  is the mass of the particles being accelerated. The frequency of the oscillator is  $c/\lambda$  and for a time of flight of half a cycle, the length of drift tube  $n$  must therefore be

$$L_n = \frac{1}{2} v_n \lambda / c = \frac{1}{2} \beta_n \lambda \quad (4.5)$$

so that for non-relativistic energies, from (4.4) and (4.5)

$$L_n \propto n^{1/2}$$

It also follows that if the energy gain per gap is held constant the accelerator length is directly proportional to wavelength. The particles emerge in bunches corresponding closely with the times of appearance of the gap voltage  $V$ , at which resonance is possible.

The apparent requirement that the drift-tube structure should be designed for exact resonance with the accelerating beam was realized to be unnecessary following the enunciation of the principle of *phase stability* by McMillan and by Veksler in 1945. In its application to the linear accelerator (Fig. 4.4) this principle considers a particle that crosses a gap with a phase angle  $\phi_s$  with respect to the accelerating voltage waveform (point A). If  $\phi_s$  corresponds to the voltage  $V$  (eqn (4.4)) for which the drift-tube structure is designed, then the particle arrives at the next gap with the same phase angle. Late particles, however, ( $\phi > \phi_s$ , points B) receive a larger acceleration in the gap, traverse the drift tube more quickly and move towards point A in phase at the next gap. Similarly, early particles

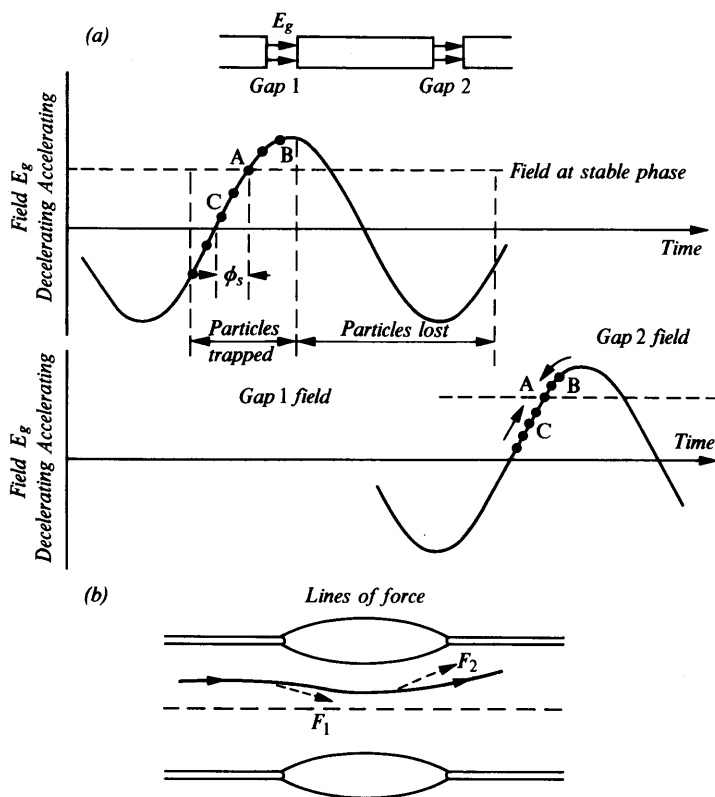


Fig. 4.4 (a) Phase stability in a drift-tube ion accelerator. The dots show the phase angles with respect to the gap field of a bunch of particles of uniform velocity arriving at gap 1. At gap 2 there is increased bunching about the stable phase  $\phi_s$ . (b) Radial defocusing of particles passing through a cylindrical gap in a field increasing with time.

( $\phi < \phi_s$ , points C) will be less accelerated and will also move towards A in phase. Particles corresponding to point A thus have stable phase, and all particles with phase angles within a certain range of  $\phi_s$  will be trapped and will oscillate about the point of stable phase. Latitude is therefore possible in the mechanical tolerances that must be applied to the drift-tube structure.

The desirable feature of axial (phase) stability leads to *radial instability* because the stable phase point is on the rising part of the voltage wave. Figure 4.4*b* illustrates this; because the field increases as the particle traverses the gap, the defocusing force predominates. Radial stability is now generally restored by means of quadrupole magnets within the drift tubes themselves.

The original mode of excitation indicated in Fig. 4.3 is now used only for low-energy accelerators. For energies above, say, 5 MeV for protons, the availability of high powers at microwave frequencies makes it highly desirable to use the resonant-cavity type of excitation introduced by Alvarez (Fig. 4.5). The cavity is tuned by radius, rather than length, and is excited in the lowest longitudinal mode, with a uniform axial electric field throughout its length. The drift tubes divide the cavity into  $n$  sections and the particles traverse the successive drift tubes while the field is in the decelerating phase,

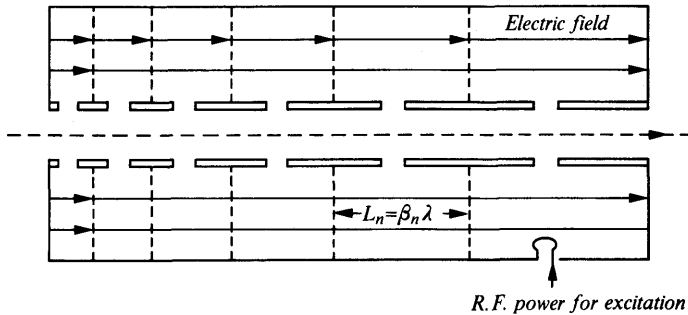


Fig. 4.5 Alvarez resonant accelerator.

receiving acceleration at the gaps. The section length  $L_n$  increases with particle velocity according to the equation

$$L_n = v_n \lambda / c = \beta_n \lambda \quad (4.6)$$

since the particles traverse one complete section in each cycle. The high radiofrequency power required to excite the cavity is not usually supplied continuously and the accelerator is operated from a pulsed transmitter with a duty cycle (on-off ratio) of about 1 per cent. A d.c. injector supplies ions of energy 500–4000 keV to the



main accelerator, and an improvement in intensity is sometimes obtained by incorporating a special cavity to 'bunch' the injected beam at approximately the selected stable phase angle of the main radiofrequency field.

Linear accelerators have been built both for protons and for heavier ions; the principle is similar in each case. For a given structure and wavelength, equation (4.6) requires that the velocity increments at each accelerating gap should be the same for each particle. A range of values of  $Ze/M$ , corresponding to different heavy ions, in different charge states, can therefore be accelerated by adjusting the radiofrequency voltage so that the gap field  $E$  is proportional to  $M/Z$ . The performance of the Alvarez proton accelerator at Berkeley is shown in Table 4.1.

The main advantages of the linear accelerator as a source of nuclear projectiles are the good collimation, the high homogeneity, the relatively high intensity of the beam and the possibility of extension of the machine to extremely high energies. A disadvantage for experiments requiring coincidence counting is the sharply bunched nature of the output, which increases the ratio of random to real coincidences in the counter systems. It is also difficult, though not impossible, to vary the output energy and in this and the preceding respect the linear accelerator is much inferior to the electrostatic generator. The major technical limitation in the extension of linear accelerators towards higher energies and higher intensities is in the development (and maintenance) of the necessary high-power oscillators. It is possible, however, that the situation will be completely transformed by the development of *superconducting* (cryogenic) accelerators in which the power dissipation will be very small.

TABLE 4.1 Performance of linear accelerators

<i>Machine</i>	<i>Berkeley proton accelerator<sup>1</sup></i>	<i>Stanford electron accelerator (SLA)<sup>2</sup></i>
Energy	31.5 MeV	20 GeV
Sectionalization	47 drift tubes	960 × 3.05 m coupled sections
Length	12 m	3 km
Frequency	202.5 MHz	2850 MHz
Pulse length	400 μs	2.5 μs
Pulse repetition rate	15 Hz	1–360 Hz
Peak power input	2.3 MW	245 × 16 MW
Shunt impedance	280 MΩ	53 MΩ m <sup>-1</sup>
Mean current	1 μA	30 μA
Energy spread	0.5%	1.3%

<sup>1</sup> Alvarez, L. W. *et al.*, *Rev. Sci. Instrum.*, **26**, 111, 1955.

<sup>2</sup> Neal, R. B., *Physics Today*, **20**, April 1967, p. 27.

### 4.2.2 Waveguide accelerators

A standing-wave pattern in a cavity, such as that developed in the ion accelerator (Sect. 4.2.1), may also be regarded as a superposition of two progressive waves moving in opposite directions. One of these waves travels with the particles and accelerates them. This suggests the feasibility of an equivalent form of accelerator in which particles are continuously accelerated by a progressive wave in a metal guide. If the particles are moving with a relativistic velocity, the wavelength of the radiofrequency field is constant; the energy conveyed to the particles increases their total mass rather than accelerating them. Waveguide accelerators are especially suitable for electrons since these particles have a velocity of  $0.98c$  for an energy of only 2 MeV, which may easily be provided at injection by an electrostatic accelerator.

In familiar types of waveguide the phase velocity of the travelling wave is always greater than the velocity of light but may be reduced by loading the guide with a series of diaphragms (Fig. 4.6). Electrons move in bunches near the peak field of the travelling wave and

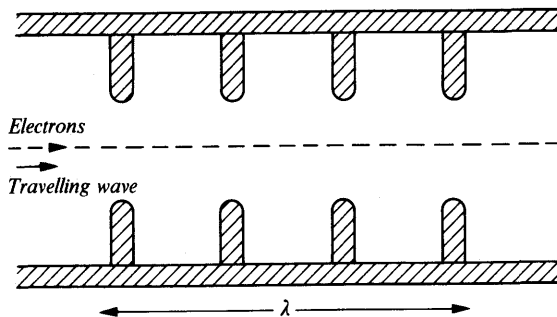


Fig. 4.6 Disc-loaded circular waveguide.

gain energy continuously from the wave. At velocities approaching the velocity of light radial defocusing forces vanish (since there is compensation between effects due to the electric and magnetic fields in the guide) and there is no definite axial stability, so that good quality of mechanical construction is necessary.

Travelling-wave accelerators usually operate from pulsed magnetrons or klystron amplifiers with a wavelength of about 0.1 m. In the remarkable 3-km Stanford linear accelerator (SLA), whose performance is shown in Table 4.1, power is fed into a disc-loaded waveguide of high mechanical precision from 245 klystron amplifiers driven in synchronism from a master oscillator. Electrons are injected into a short tapered section in which the phase velocity and longitudinal accelerating field both increase, and are bunched at a

phase near the peak field of the travelling wave. Phase oscillations are damped by the effect of the rapidly increasing mass and the bunch moves through the main length of uniformly loaded guide with the velocity of light. No auxiliary focusing is used but despite this a beam is obtained, once perturbing magnetic fields have been neutralized, at the end of the guide. This is possible because of the relativistic shortening of the guide in the electron frame of reference; from the point of view of an observer at rest with respect to the electron the guide appears to be less than 1 m long and there is not much time for lateral divergence. The machine is supplied with microwave power from the klystrons in pulses of  $2.5 \mu\text{s}$  length. About half this time is required to build up the fields in the guide and electrons are injected and accelerated during the remaining part of the pulse.  $\downarrow$

$\downarrow$  Electron linear accelerators may also be used to produce and to accelerate positrons. A heavy-metal radiator is placed in the electron beam at an intermediate point along the accelerator and the positrons emerging (as a result of direct production or photoproduction via bremsstrahlung) can be accelerated if the phase of the travelling wave is adjusted. The positrons and electrons from the same accelerator, can be used to provide bunches of particles in storage rings for the study of  $(e^+e^-)$  collisions. Two-quantum annihilation of the positrons in flight can be used to furnish a beam of homogeneous photons.  $\downarrow$

$\downarrow$  The electron linear accelerator,  $\downarrow$  as shown by the figures in Table 4.1,  $\downarrow$  is a machine of poor duty cycle compared with that of orbital accelerators (Sect. 4.3)  $\downarrow$  and it is expensive in radiofrequency power although superconducting techniques will improve performance substantially. Upward extension of energy is not limited by the radiative losses inherent in orbital-electron accelerators, but physical length obviously becomes excessive for energies much above that of the SLA (Table 4.1).

### 4.3 Orbital accelerators (Ref. 4.3)

#### 4.3.1 General

As noted in Sections 1.2.6 and 2.1.1, a particle of mass  $M$  and charge  $e$  moving with constant speed  $v$  in a plane perpendicular to the lines of force of a uniform magnetic field of flux density  $B$ , is acted on by a constant force at right angles to its velocity vector and describes a circle of radius  $r$  given by

$$evB = \gamma Mv^2/r \quad (4.7)$$

where  $\gamma = (1 - v^2/c^2)^{-1/2} = (1 - \beta^2)^{-1/2}$ . The momentum of the particle is

$$p = \gamma Mv = eBr \quad (4.8)$$

and its angular velocity is

$$\omega = v/r = eB/\gamma M \text{ rad s}^{-1} \quad (4.9)$$

The frequency of rotation in the circular orbit, known as the *cyclotron frequency*, is

$$\begin{aligned} f &= \omega/2\pi = eB/2\pi\gamma M \\ &= 15.25 \text{ MHz per tesla for protons for } \gamma = 1 \text{ (} f = f_0 \text{)} \end{aligned} \quad (4.10)$$

If the field is uniform azimuthally, but non-uniform radially, the axial component at radius  $r$  may be written

$$B_z = B_0(r_0/r)^n \quad (4.11)$$

where  $B_0$  is the flux density at a reference radius  $r_0$ . The *field index* is

$$n = -(r/B_z) \partial B_z / \partial r \quad (4.12)$$

and the frequencies of axial and radial oscillation about an equilibrium orbit of radius  $r_0$  are

$$\begin{aligned} f_z &= f_0(n)^{1/2} \\ f_r &= f_0(1-n)^{1/2} \end{aligned} \quad (4.13)$$

For the orbit to be stable it is necessary for  $n$  to be between 0 (uniform field) and 1.

The total energy of the particle, omitting any potential energy term, and setting  $c = 1$ , is given by

$$\begin{aligned} E &= \gamma M = (p^2 + M^2)^{1/2} \\ &= [(eBr)^2 + M^2]^{1/2} \end{aligned} \quad (4.14)$$

and the kinetic energy  $T$  is given by

$$T + M = E,$$

or

$$T(T + 2M) = p^2 = (eBr)^2$$

In the non-relativistic approximation  $T \ll M$  and

$$T \rightarrow p^2/2M \quad (4.15a)$$

while for extreme relativistic velocities  $T \gg M$  and

$$T \rightarrow E \rightarrow eBr \quad (4.15b)$$

Equation (4.14) gives the total energy of a particle moving at radius  $r$  in an orbital accelerator in which the magnetic flux density at the orbit is  $B$ . The way in which the final energy is attained in two different types of accelerator will now be described.

### 4.3.2 The isochronous cyclotron (fixed field, fixed frequency)

The cyclotron is a magnetic resonance accelerator developed by Lawrence and his collaborators in Berkeley in the 1930s.

From equation (4.10) it is clear that for energies  $\ll Mc^2$ , i.e. when  $\gamma$  is very close to unity, the cyclotron frequency  $f$  for a particle of charge  $e$  and mass  $M$  moving in a field  $B_0$  is constant and equal to  $f_0$  (isochronous motion). An oscillating electric field with a frequency  $f_0$  may then be applied to increase the energy of the circulating particles. This is achieved in practice by the radiofrequency excitation of a D-shaped electrode (two dees in most early cyclotrons) in the vacuum system in which the particles move (Fig. 4.7a). The particles, under present assumptions, are synchronous with the radiofrequency electric field and receive an acceleration causing an increase in orbit radius twice per revolution, at entry to and exit from the D-electrode. At the maximum radius  $R$  the kinetic energy is

$$T = p^2/2M = e^2 B_0^2 R^2 / 2M \quad (4.16)$$

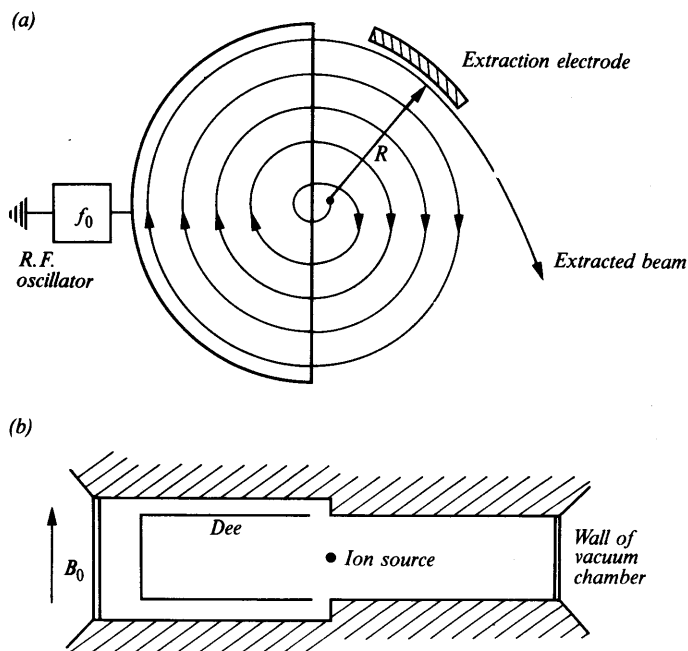


Fig. 4.7 The isochronous cyclotron. (a) Path of ions in a cyclotron from central ion source to extracted beam. (b) Vertical section showing dee and wall of vacuum chamber. The section indicates an azimuthal variation of the main field  $B_0$  (see text).

and the particles may be extracted by the application of suitable deflecting fields. If *negative* ions are accelerated, extraction is simplified by the use of a stripping foil to reverse their charge and curvature.

There is no phase stability in a uniform-field cyclotron although bunching occurs early in the acceleration process and is maintained, at about a 10 per cent duty cycle, during the passage to maximum radius. Axial and radial stability require  $0 < n < 1$  (eqn (4.13)) during the main acceleration, i.e. a radially *decreasing* magnetic field as shown in Fig. 4.8a. Unfortunately, this destroys isochronism (eqn (4.10)) and the effect is accentuated by the fact that  $\gamma$  is gradually increasing above 1 as the particle velocity increases. The conventional cyclotron is, therefore, limited in output energy; the performance of a typical machine is shown in Table 4.2.

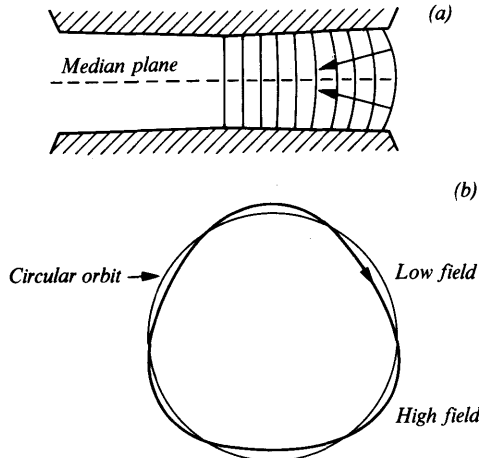


Fig. 4.8 The isochronous cyclotron. (a) Axial forces in radially decreasing cyclotron field. (b) Closed orbit in azimuthally varying field.

Although it is possible because of the principle of phase stability to design a cyclotron (*synchrocyclotron*) in which synchronism can be preserved by a programmed decrease of the frequency  $f$  of the electric field, it is preferable to use a magnetic field shape that permits the radial *increase* required for isochronism, but provides some extra focusing forces. The radial variation of mean field required is found from equation (4.10) to be

$$B = \gamma B_0 = B_0 / (1 - \beta^2)^{1/2} \quad (4.17)$$

and approximately this gives

$$B = B_0 (1 + \frac{1}{2} \beta^2) = B_0 (1 + r^2 \omega_0^2 / 2c^2) = B_0 (1 + 2\pi^2 f_0^2 r^2 / c^2) \quad (4.18)$$

The extra focusing is obtained, following a suggestion of L. H.

Thomas, by introducing *azimuthal variation* into the field, as already indicated in Fig. 4.7*b*. In such a field, also known as *sector-focusing*, there are alternate high and low field regions. A closed orbit in this field is non-circular, as shown in Fig. 4.8*b*, and as a particle in such an orbit crosses a sector boundary (either high  $\rightarrow$  low or low  $\rightarrow$  high) *radial* components of velocity arise. The field variation at the boundaries gives rise to *azimuthal* components and the new  $\mathbf{v} \times \mathbf{B}$  force is axially focusing in both types of transition region. The sector focusing may be improved by using spiral instead of radial sector boundaries. Several such cyclotrons with design energies of the order of 100 MeV for protons are now operating.

TABLE 4.2 Performance of orbital accelerators

Machine	Particle energy /MeV	Orbit diameter /m	Orbital frequency /MHz	Pulse repetition rate/Hz	Output current or particles per pulse	Magnet weight / $10^3$ kg
Fixed frequency cyclotron (Birmingham) <sup>1</sup>	20 (d)	1.5	10.3	—	500 $\mu$ A	254
AG proton synchrotron (CERN) <sup>2</sup>	27 000 (p)	200	—	0.3	$>2 \times 10^{12}$	3450

All accelerators operating with radiofrequency fields exhibit a fine time-structure of the beam on a scale determined by the radiofrequency.

Note: p = protons, d = deuterons

<sup>1</sup> *Nature* **169**, 476, 1952.

<sup>2</sup> Adams, J. B., *Nature* **185**, 568, 1960.

#### 4.3.3 The synchrotron (variable field)

The construction of an/ isochronous/ cyclotron for the multi-GeV range of energies would be prohibitively expensive. It is therefore necessary to design a phase-stable accelerator in which the particles are held in a mean orbit of constant radius from initial to final energy. Only an annular magnet is then required, but the guiding magnetic field must increase to match the increasing momentum of the circulating particles; these gain energy from a radiofrequency cavity through which they pass.†

† The main components of a synchrotron are sketched in Fig. 4.9, together with a typical magnetic field cycle.† Particles injected into the magnet ring from a linear accelerator pass through the radio-frequency accelerating cavity and are ejected by a pulsed extraction magnet if required as an external beam.†

† Alternatively, the circulating beam may be directed at the end of the magnet cycle to an internal target from which secondary beams of particles such as photons, pions, kaons or hyperons may be

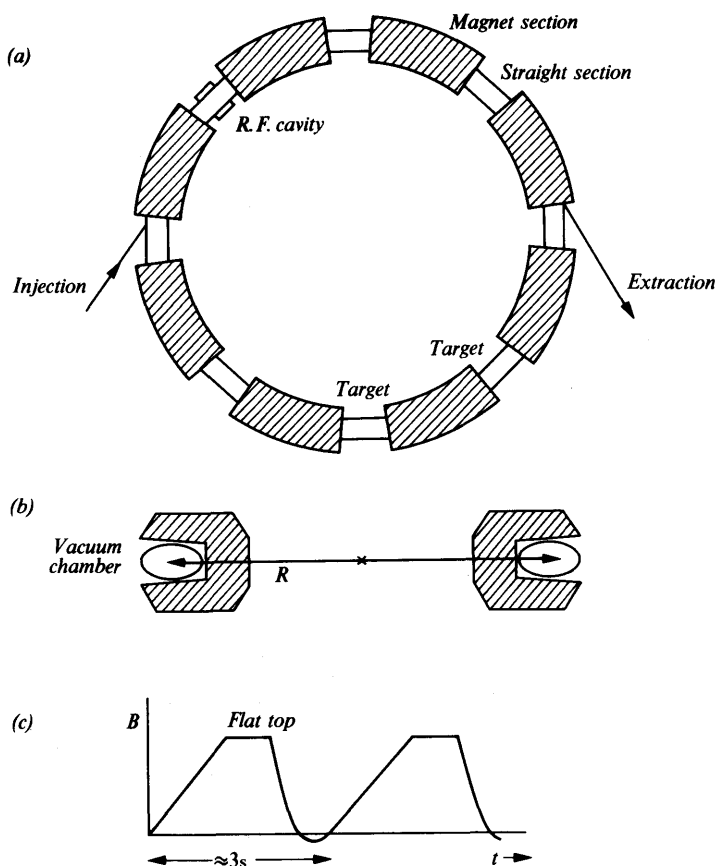


Fig. 4.9 The weak-focusing proton synchrotron. (a) Magnet ring. (b) Cross-section through magnetic sector. (c) Magnetic field cycle, showing flat top to give a long 'spill-time' of extracted beam.

obtained. Injection, acceleration, extraction and target equipment is conveniently located in the straight sections forming part of the magnet ring.

The momentum corresponding to a magnetic induction  $B$  and a radius  $R$  is given by equation (4.8) and inserting numerical values

$$p/(\text{Gev}/c) = (0.3B/\text{tesla})(R/\text{metre}) \quad (4.19)$$

For relativistic particles this is also the total energy  $E$  in GeV, so that for 1 km radius, which applies to the 400-GeV proton synchrotron (SPS) at CERN, Geneva, a magnetic induction of 1 T corresponds to an energy of 300 GeV. The acceleration frequency is constant in the relativistic region.



[In *weak focusing* (*constant gradient* or CG) synchrotrons, radial and axial stability of the beam is achieved by use of a field index between 0 and 1 uniformly in each magnetic sector of the ring except for edge regions.] A major advance in accelerator design was made [in 1951–53] when [Christofilos, and also Courant, Livingston and Snyder realized that it is not necessary to render the axial and radial oscillations stable simultaneously. In the *strong focusing* (*alternating gradient* or AG) synchrotron alternate magnetic field sectors have reversed field gradients, i.e.  $n \gg 1$  and  $n \ll 1$  (negative) so that there is either axial or radial focusing but not both simultaneously in a given sector. There is, however, *net* focusing in both directions after passage through two sectors (cf. the achromatic lens combination in optics). The advantage of AG focusing is that because the free oscillation periods shown in equation (4.13) become much shorter the amplitudes are reduced and a considerable spread in momentum can be accommodated in a small radial space, with consequent saving of magnet and vacuum chamber costs. The engineering design of an AG synchrotron may use either *combined* function magnetic sectors in which bending and focusing both take place, or *separated* function component fields.]

[The particle motion is phase-stable in synchrotrons. In weak focusing machines a particle arriving early (B) at the accelerating gap (Fig. 4.10) receives a greater energy than it should and moves to a slightly greater radius for which an orbit takes *longer* to describe. At the next transit of the accelerating cavity it has, therefore, moved towards the phase-stable point A. Similarly, late particles (C) also

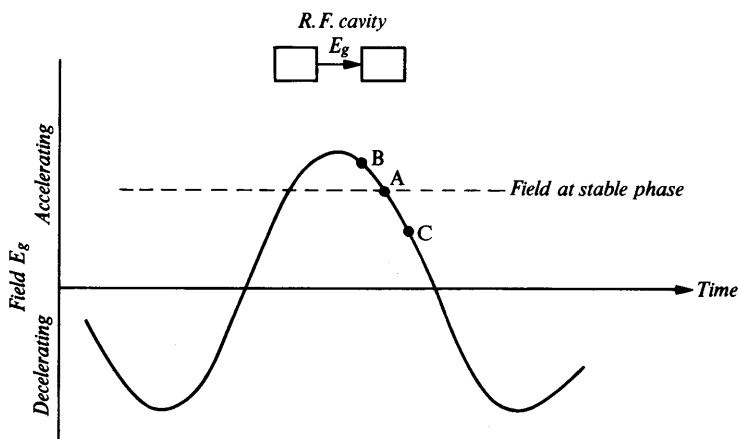


Fig. 4.10 Phase stability in a weak focusing (CG) synchrotron; particles arriving at times B and C move towards time A, relative to the voltage wave, as acceleration proceeds.

move towards A, which is on the *falling* part of the cavity-voltage waveform in contrast with the situation for linear accelerators (Fig. 4.4). While these phase changes are taking place the magnetic field of the accelerator is rising, and the radiofrequency is falling if the particles are non-relativistic, so that the phase-stable point A always corresponds with an increasing energy./

/In strong focusing machines, because of the large value of  $n$ , the change of radius with momentum is rather small and the orbit for late particles at low energies may actually take a shorter time to describe. The phase-stable point is then on the *rising* part of the voltage wave, as with linear accelerators. Above a certain energy known as the transition energy, however, the orbit for late particles begins to take a longer time to describe than that for the synchronous beam and the phase-stable point then moves to the falling part of the voltage wave as for CG machines./The performance of the CERN PS (proton synchrotron) is shown in Table 4.2.

/The highest-energy proton accelerators now existing (FNAL 500 GeV, CERN SPS 400 GeV) are AG machines./ So is the highest-energy orbital electron accelerator (Cornell 10 GeV), but this is a lower energy than that of the Stanford linear accelerator (20 GeV) because of the severe and fundamentally unavoidable radiation loss in electron synchrotrons. Electrons moving at radius  $R$  with energy  $E$  suffer an energy loss per turn proportional to  $E^4$  and

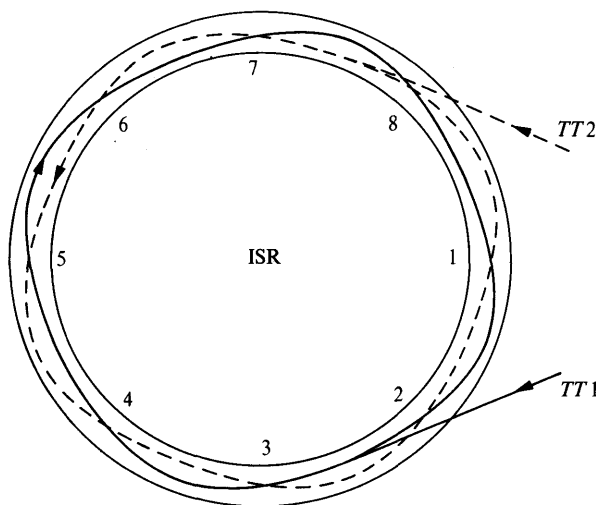


Fig. 4.11 Intersecting proton beams in the CERN storage rings (ISR). The oppositely circulating beams are sent from a proton synchrotron through the transfer tubes TT1 and TT2 into high-vacuum systems with a separate ring of magnets for each beam. Experiments are conducted at the intersections 1-8.

ultimately the radiofrequency circuit is unable to supply the losses, so that no further energy increment is possible. The *synchrotron radiation* produced in this way now forms an intense spectroscopic source from the X-ray region to the infra-red.

Because of the limitation due to radioactive losses, electron synchrotrons are not designed for exceptionally high magnetic fields and the magnet cycle can be much more rapid, and the mean particle intensity greater, than in proton synchrotrons. Both machines produce a beam in which there is radiofrequency bunching within pulses of a repetition rate determined by the modulation cycle. By programmed control of the magnetic field and extraction fields, a long 'spill time' for the extracted beam, suitable for counter experiments, can be obtained (Fig. 4.9c).

The beams from high-energy proton and electron synchrotrons (and from the Stanford electron linear accelerator) have been used to fill *storage rings* in which they can circulate for long periods without loss if the pressure in the ring is low enough. If oppositely moving beams of energy  $E$  and mass  $M$  are made to intersect in storage rings (Fig. 4.11) the energy available in the centre-of-mass system is just  $2E$  compared with  $\sqrt{2M(E \pm M)}$  for a collision with a target particle at rest in the laboratory. Electrons in storage rings also radiate and losses must be made up from a radiofrequency cavity. Such electron rings are very attractive as sources of synchrotron radiation.

It is possible to inject positrons, generated electromagnetically in a target bombarded by electrons, into an electron ring in which they circulate in a direction opposite to the electrons. Study of the ( $e^+e^-$ ) collision in this way has revealed much information on the new  $J/\Psi$  particles (Sect. 2.2.3).

## 4.4 Bending and focusing magnets

Magnets are used extensively in beam handling at all energies and also as spectrometers when the highest possible resolution is required. The design of such elements is related to that of accelerator magnetic sectors.

### 4.4.1 The magnetic spectrometer

Suppose that charged particles of uniform momentum  $p$  from a point source  $S$  move in a plane perpendicular to the lines of force of a uniform magnetic field in which the radius of curvature of their path is  $\rho$  so that, by equation (4.8)

$$\rho = p/eB \quad (4.20)$$

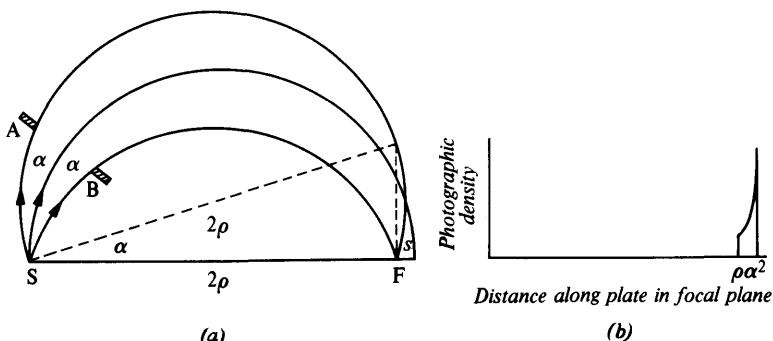


Fig. 4.12 First-order focusing after  $180^\circ$  deflection of charged particles in a uniform magnetic field.

if the particles are singly charged. Geometrically, as shown in Fig. 4.12, the paths of such particles converge to a focus F of finite width  $s$  determined by the angular width  $2\alpha$  of the cone of particles selected, for instance, by an aperture AB. From the figure

$$s = 2\rho(1 - \cos \alpha) \approx \rho\alpha^2 \quad (4.21)$$

and the focus, in the plane, is said to be of *first order*.

The *resolution in momentum* is the relative change in momentum necessary to shift the line from a point source by its own width, i.e.

$$R = \Delta p/p = \Delta\rho/\rho \quad \text{for} \quad \Delta\rho = s$$

so that  $R = \alpha^2/2$  from (4.21), while the *dispersion*, defined as the change in line position per unit relative momentum change, is

$$\begin{aligned} D &= d(2\rho)/dp/p = 2\rho \, dp/dp \\ &= 2\rho \quad \text{from (4.20)} \end{aligned}$$

In practice the line width observed includes a contribution from finite source width which generally exceeds the geometrical aberration  $\rho\alpha^2$ .

If both source and detector are contained within the magnetic field and if the field itself is known to high accuracy, the semicircular spectrometer can be operated as an instrument of high precision. For nuclear reaction experiments it is often desirable to sacrifice precision to the requirements of intensity, and then an inhomogeneous field (eqn (4.11)) which provides focusing both radially and axially may be used. This *double focusing* condition is achieved when the wavelengths of the radial and axial oscillation are equal, and in terms of frequencies equation (4.13) then gives  $n = \frac{1}{2}$ ,  $f_z = f_r = f_0/\sqrt{2}$ . The paths converge to a focus after a deflection angle of  $\sqrt{2}\pi = 254.6^\circ$ .

Focusing is also obtainable, with a smaller angle of deflection, when the source and detector are outside the boundaries of the magnetic field. Such magnets are convenient for use with accelerators but require careful calibration when used in precision experiments because of the effects of fringing fields. These fields can, however, be turned to advantage in reducing aberrations if the pole of the spectrometer is split into two sections as suggested by Enge. In high-resolution studies of nuclear reaction products, the spectrometer design must also allow for the kinematic shift due to the variation of particle energy over the angular acceptance of the instrument.

All types of magnet with simple dipole fields and beam width control by slits are used extensively for beam deflection, and in high-energy physics for defining a 'momentum bite'  $\Delta p/p$  when an accelerator produces a secondary beam of product particles with a range of momenta.

#### 4.4.2 The magnetic quadrupole lens

A magnet with four poles of hyperbolic contour, arranged as shown in Fig. 4.13a, transmits axial particles without deflection. An off-axis charged particle, however, finds itself in a magnetic field whose potential is

$$V \propto r^2 \sin 2\theta \quad (4.22)$$

where  $r$  and  $\theta$  are shown in the figure. The deflecting force for paraxial particles is always proportional to the distance of the particle trajectory from the axis and is directed towards the axis for particle trajectories with a small angle  $\theta$  to one of the planes separating the poles and away from the axis for trajectories with a small angle to the perpendicular plane.

A pair of such quadrupoles set with an angular displacement of  $\pi/2$  may be adjusted to provide net focusing in both planes (though with different focal lengths in general) because the diverging effect produced in one plane by the first element leads to trajectories further from the axis in the second element. For these the deflecting force is stronger and of opposite sign, so that there is overall focusing.

Magnetic quadrupoles are widely used for concentrating charged particle beams. In high-resolution spectroscopy, a quadrupole element may be combined with dipole deflections to increase the solid angle of acceptance; such spectrometers are known as QD instruments. Since an inhomogeneous magnetic field deflects a magnet, quadrupoles can also be used for neutral atomic beams providing that there is a resultant electronic magnetic moment.

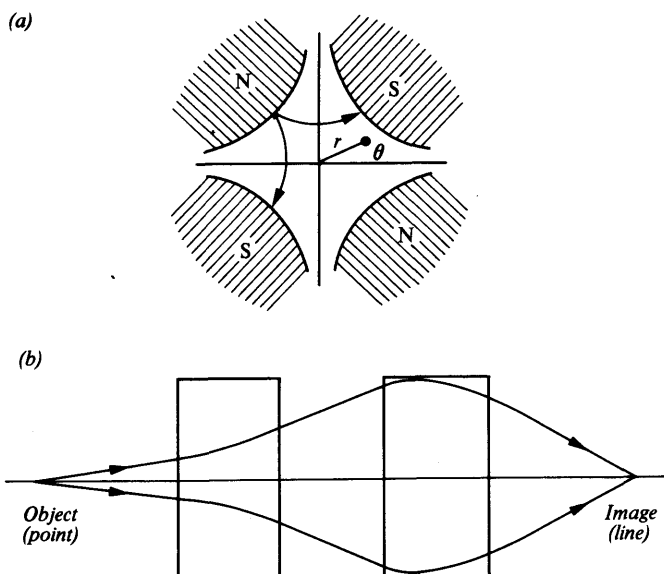


Fig. 4.13 The magnetic quadrupole. (a) Cross-section through poles, showing the  $(r, \theta)$  coordinates of a paraxial trajectory. (b) Quadrupole doublet, showing net focusing in one plane by the diverging-converging fields. In the perpendicular plane the fields are converging-diverging and the focal length is different so that the lens is in general astigmatic, with two focal lines.

Electrostatic quadrupole lenses operate in a similar way to magnetic elements and are used, for instance, in the drift tubes of linear accelerators.

## 4.5 Detectors (Ref. 4.4)

Nuclear detectors of single particles are required to determine one or all of the quantities position, angle of trajectory, momentum, velocity, energy and charge. Some of the general techniques used, often involving combinations of detectors, have already been described in Section 3.2.5 as examples of the application of the stopping-power formula. In this section a brief account is given of some of the main types of individual instrument.

### 4.5.1 The scintillation counter

The development of the modern scintillation particle-counting system from the original zinc sulphide screen viewed by a microscope,

as used by Rutherford, is due firstly to the application of the photomultiplier as a light detector (Curran and Baker) and secondly to the discovery of scintillating materials that are transparent to their own fluorescent radiations (e.g. anthracene by Kallman and sodium iodide by Hofstadter).

The processes resulting in the emission of light when a charged particle passes through matter depend on the nature of the scintillating material. Inorganic crystals such as NaI are specially activated with impurities (e.g. thallium) to provide luminescence centres in the band gap. Electrons raised from the valence band of the crystal by Coulomb interaction may themselves excite an electron in a luminescence centre. This excitation will take place, preferentially, in accordance with the Franck–Condon principle, so that the relevant interatomic spacing in the centre is left unchanged (Fig. 4.14,

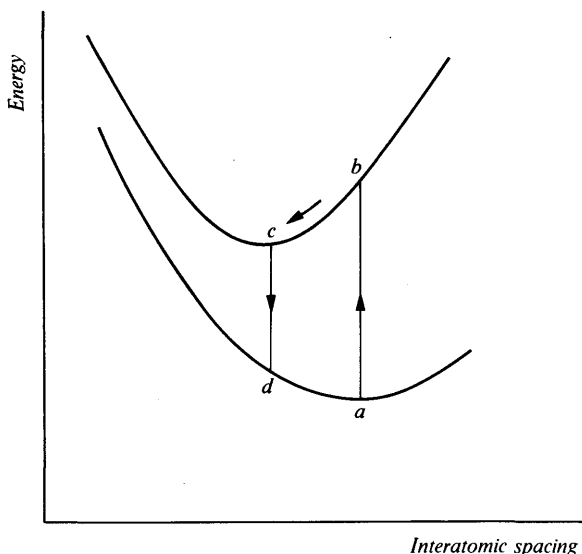


Fig. 4.14 Franck–Condon principle. The two curves are the energies as a function of an interatomic spacing of different electronic levels of a luminescence centre. The principle asserts that radiative transitions tend to leave the interatomic distance unchanged. The transition ( $bc$ ) is non-radiative.

transition  $ab$ ). It is followed by a radiationless transition  $bc$  and then by photon emission  $cd$ , also preserving interatomic spacing. The fluorescent radiation is of a longer wavelength than that corresponding to the absorption transition  $ab$  and is thus not usually re-absorbed by the scintillator. In the case of organic scintillators, molecular electrons are excited directly to one of several singlet levels and make radiationless transitions to the lowest excited singlet

level. From this, fluorescent radiation to the vibrational substates of the ground state takes place, independently of the initial excitation process, and without the intervention of any activator, so that the light pulse is generally faster than with inorganic materials.

The scintillators chiefly used for particle or photon detection are:

(i) *Sodium iodide* (thallium activated). Because of high density this is an efficient scintillator for gamma-ray detection. The decay time of the light pulse from the luminescence centres is about  $0.25 \mu\text{s}$ , with a longer component of about  $1.5 \mu\text{s}$ .

(ii) *Plastic and liquid scintillators*. These are readily obtainable in very large volumes and can be adapted to many different geometrical arrangements, including counting of a source over a solid angle of  $4\pi$ . The scintillator often contains a wavelength shifter to degrade the emitted spectrum to a wavelength that is transmitted efficiently through the crystal and that matches a photomultiplier detector. The light pulse associated with an instantaneous burst of ionization decays very rapidly, with a time constant of about  $0.005 \mu\text{s}$ , so that these scintillators are useful for fast counting.

The scintillator is placed directly on the window of a photomultiplier tube (Fig. 4.15), or is coupled to it via a light guide. The window

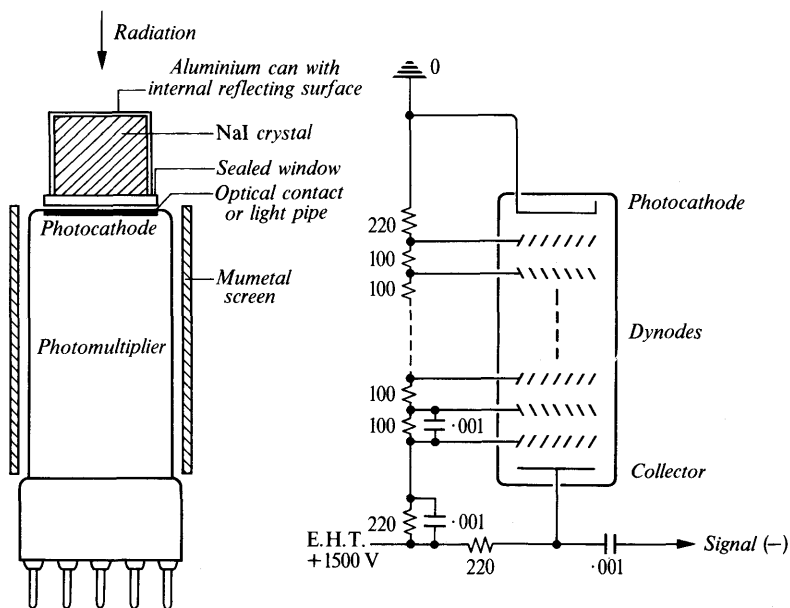


Fig. 4.15 Scintillation counter, showing circuit arrangement for supplying dynode potentials (resistances in  $k\Omega$ , capacitances in  $\mu\text{F}$ ).



is coated on the inside with a thin antimony-caesium layer from which photoelectrons are emitted with up to about 10 per cent efficiency for photons of wavelength 400–500 nm. The multiplier provides a current amplification determined by the interelectrode potential difference; external amplification may also be applied, with differentiation and integration time constants set to control the output pulse shape, essentially by defining the bandwidth of the amplifier. This should be suitable for transmitting pulses with a rise time characterized by the decay time of the luminescence centres in the scintillator. It is also necessary to minimize pulse pile-up and to discriminate as far as possible against circuit noise. In practice, the differentiation and integration time constants are usually made equal.

In the detection of  $\gamma$ -radiation by a sodium iodide scintillator an incident photon of energy, say 1 MeV, interacts with an atom or an electron of the scintillator and produces photoelectrons or Compton electrons together with lower-energy radiation which may itself interact similarly in the crystal. This primary process, converting photon energy into electron energy, takes place in  $\approx 10^{-10}$  s, with an efficiency, as far as photon detection is concerned, determined by the absorption coefficient of the material, e.g. about 30 per cent for a cylindrical crystal of 25 mm  $\times$  40 mm diameter. The primary electrons excite radiation from the luminescence centres and the fluorescent radiations eject photoelectrons from the photocathode of the multiplier. When all efficiency factors are included, the 1-MeV incident photon may produce only about 2000 photoelectrons, with an associated statistical fluctuation of  $\sqrt{2000}$ , i.e. 2 per cent. The resulting spread of the final output pulse-height distribution, assuming that all radiations are completely absorbed in the scintillating crystal, is further increased by variations in the dynode multiplication factor and by variations in the efficiency of light collection over the detector volume. In practice, the pulse-height distribution for a homogeneous radiation of energy  $E_\gamma = 1$  MeV gives a resolution of about 10 per cent. The contribution to the resolution due to statistical fluctuations is expected to vary as  $E_\gamma^{-1/2}$  and the mean pulse height is closely proportional to the energy  $E_\gamma$ . The spectra observed with a pulse-height analyser for radiations from  $^{57}\text{Co}$ ,  $^{137}\text{Cs}$  and  $^{22}\text{Na}$  detected by a sodium iodide crystal of dimensions 25  $\times$  40 mm are shown in Fig. 4.16. Their characteristic features are determined by the relative probabilities of the basic photon interaction processes in the crystal. For  $^{57}\text{Co}$ ,  $E_\gamma = 122$  keV, there is a full energy peak due to the production of photoelectrons and the capture of all radiations resulting from the atomic vacancy produced. A much weaker, lower energy 'escape peak', indicating that sometimes the atomic K X-ray (28.6 keV for iodine) leaves the crystal, may also be resolved.

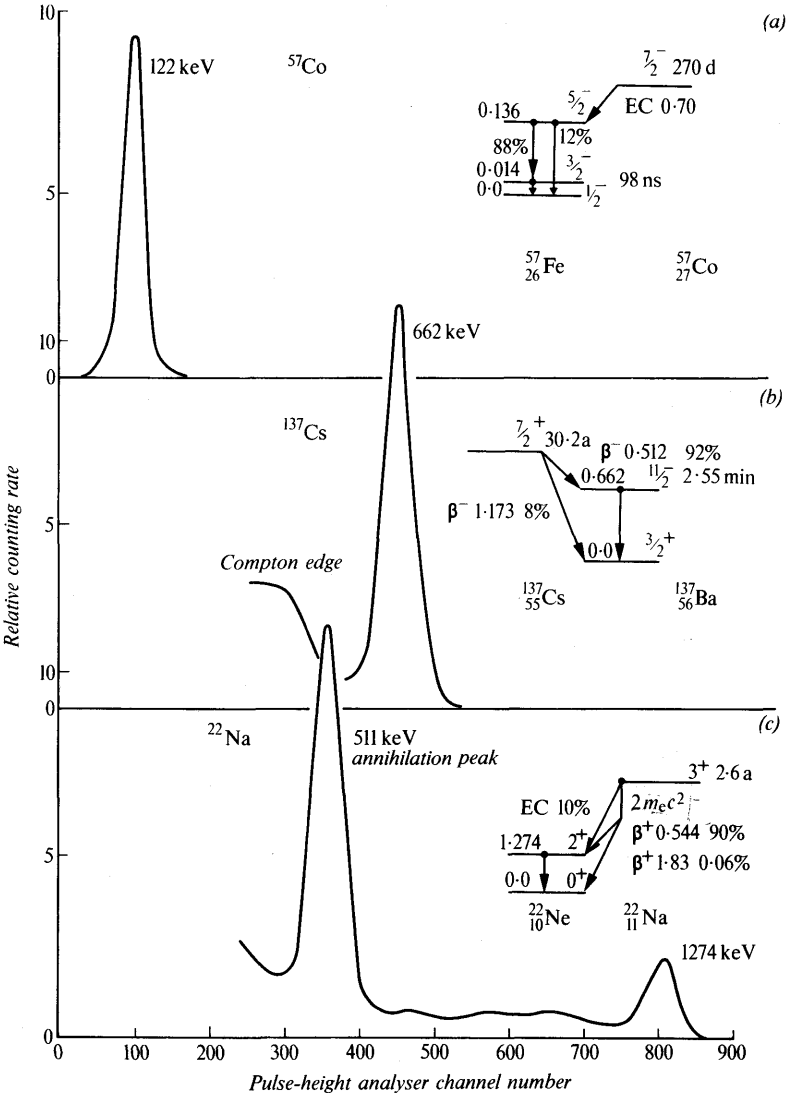


Fig. 4.16 Scintillation counter: pulse-height distribution for radiations from (a)  $^{57}\text{Co}$ , (b)  $^{137}\text{Cs}$ , and (c)  $^{22}\text{Na}$  detected in a  $25 \times 40$  mm NaI(Tl) crystal. In (a) the weak 136 keV transition is not resolved; in (b) internal conversion electrons accompany the 0.662 MeV transition but the Ba X-rays of energy 32 keV are not shown. In all spectra, peaks due to external back-scattering of forward-going photons and due to the escape of the 28.6-keV X-rays of iodine are omitted. The lifetimes shown are half-lives,  $t_{1/2}$ .

For  $^{137}\text{Cs}$ , with  $E_\gamma = 662 \text{ keV}$ , a similar full energy peak appears, but there is a contribution to this from Compton scattering and below the main peak there is a 'Compton distribution' due to recoil electrons for which the Compton-scattered photon leaves the crystal.

With  $^{22}\text{Na}$ ,  $E_\gamma = 1.27 \text{ MeV}$ , both photoelectric and Compton effects, and especially the latter, take place and in addition pair production ( $\gamma \rightarrow e^+e^-$ ) with a threshold of  $1.02 \text{ MeV}$ . The positron produced in this last effect will ultimately annihilate either in the crystal or near it, with the production (generally) of two  $511\text{-keV}$  annihilation quanta. If both of these are fully detected by the crystal, a pulse with height corresponding to  $E_\gamma$  is produced, since the annihilation energy adds to the kinetic energy of the  $e^+e^-$  pair. If one annihilation quantum escapes, there is a pulse at energy  $E_\gamma - m_e c^2$  and if both escape, one at  $E_\gamma - 2m_e c^2$ . The resulting spectrum is therefore somewhat complex even for a homogeneous photon energy. The width of the full energy peaks is seen to be  $\approx 10$  per cent.

The main advantage of the scintillator detector is that a high efficiency coupled with moderate resolution for gamma-ray detection may be obtained with  $\text{NaI(Tl)}$  in a reasonably small size and at a reasonably low cost. Organic scintillators provide excellent timing signals and can be built into the very large and complex arrays necessary for particle location and identification in high-energy physics.

#### 4.5.2 Semiconductor detectors

Solid-state detectors operate essentially through the promotion of electrons from the valence band to the conduction band of a solid as a result of the entry of the particle or photon to be detected into the solid. Since the band gap in some solids is only about  $1 \text{ eV}$ , production of an electron-hole pair as part of the general energy-loss by collision may require only  $3\text{--}4 \text{ eV}$  on average. The stopping of a particle of energy  $1 \text{ MeV}$  may thus produce  $3 \times 10^5$  electron-hole pairs and the associated statistical fluctuation would be only  $0.2$  per cent which offers a great advantage in basic resolution over the scintillation detector, and indeed over the simple gas-filled ionization chamber for which an energy expenditure of  $30 \text{ eV}$  per ion pair is required.

The difficulty in realizing the attractive features of solid-state detectors in practice has been to obtain materials in which residual conductivity is sufficiently low to permit conduction pulses due to single particles to be distinguished above background and in which the charged carriers are not rapidly 'trapped' by impurities. This

has, however, been achieved for certain *semiconductors* in: (i) junction detectors, and (ii) gamma-ray detectors.

(i) *Junction detectors for charged particles.* In an *n*-type semiconductor, conduction is due to the motion of electrons in the conduction band, and in *p*-type material the process is effectively a motion of positive holes resulting from the rearrangement of electrons between atoms in the crystal. The two materials are prepared from an intrinsic semiconductor such as silicon by the controlled addition of electron-donating or electron-accepting elements (Fig. 4.17a). In the case of intrinsic silicon these elements could be phosphorus and indium respectively and the effect of their existence within surroundings of silicon is to produce hydrogen-like structures with their own set of energy levels, known as impurity levels. These are, again respectively, slightly below the conduction band and slightly above the valence band, so that thermal excitation of electrons to the former and from the latter is readily possible. The corresponding conduction process is then by electrons (*n*-type) or by holes (*p*-type); it is assumed that all impurities are ionized.

If a junction between *p*- and *n*-type regions is formed in a crystal, then conduction electrons predominate in the *n*-region but a few will diffuse into the *p*-region (Fig. 4.17b) where the conduction electron density is low. Similarly, holes from the *p*-region will

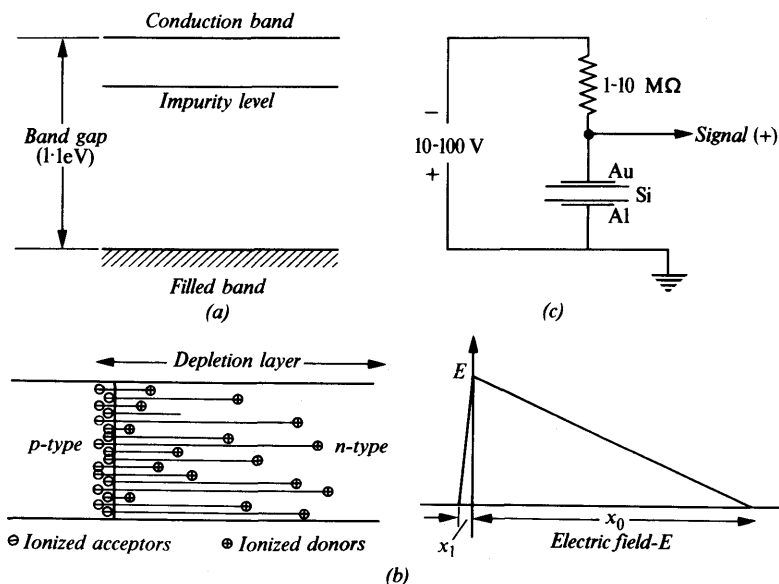


Fig. 4.17 Semiconductor counter: (a) Bands and impurity level in semiconductor. (b) Charge and electric field distributions in the depletion layer of a *p*-*n* junction. (c) Circuit arrangement (Dearnaley, G., *Contemp. Phys.*, **8**, 607, 1967).

diffuse into the  $n$ -region and the joint effect of these motions is to leave a positive space charge in the  $n$ - and a negative space charge in the  $p$ -region, near the boundary. The electric field resulting from this double layer generates a potential difference between the  $n$ - and the  $p$ -regions and this causes a drift current of thermally excited electrons or holes in the opposite direction to the diffusion current so that a dynamic equilibrium exists in which there is no net transfer of charge. The region of the crystal between the space charges has lost charge carriers in comparison with the rest of the solid and is able to sustain an electric field; it is known as the *depletion layer*.

The depth  $z_0$  of the depletion layer depends on the density of impurity centres and on any applied potential difference  $V$  (reverse bias making the  $n$ -region more positive with respect to the  $p$ -region). If  $\rho$  is the resistivity of the  $n$ -type region, then

$$z_0 \approx (\rho V)^{1/2}$$

For silicon of the highest practicable resistivity a depletion depth of about 5 mm may be obtained.

If a charged particle enters the depletion layer the electron-hole pairs produced are swept away by the field existing across the layer and a pulse may be detected in an external circuit. Because of the low value of the energy required to form an electron-hole pair, and because of the existence of another favourable factor (Fano factor  $F$ ) which recognizes that energy losses for a particle of finite energy are not wholly independent, a resolution as good as 0.25 per cent is obtainable at 5 MeV. Figure 4.18 shows the spectrum of  $\alpha$ -particles from  $^{212}\text{Bi}$  observed with a silicon detector of resistivity 27  $\Omega\text{m}$ .

Two types of  $p$ - $n$  detector have been developed:

- (a) *the diffused junction* detector in which a donor impurity, usually phosphorus, is introduced into a  $p$ -type (boron doped) silicon single crystal to form a depletion layer at the diffusion depth; and
- (b) *the surface barrier* detector in which a  $p$ -type layer is formed on the surface of  $n$ -type silicon by oxidation. Contact is made to the detectors through a layer of gold. The counter base is often a layer of aluminium. Signals are derived from the surface barrier detector by the connections shown in Fig. 4.17c. Since the depth of the depletion layer, and consequently the inter-electrode capacitance, depends on the applied voltage, a charge-sensitive rather than voltage-sensitive pre-amplifier is used. Semiconductor counters are not themselves amplifying, and a typical output voltage might be 20 mV for a particle of energy 5 MeV.

The advantages of the silicon  $p$ - $n$  junction as a detector of heavy particles are its excellent resolution and linearity, its small size and

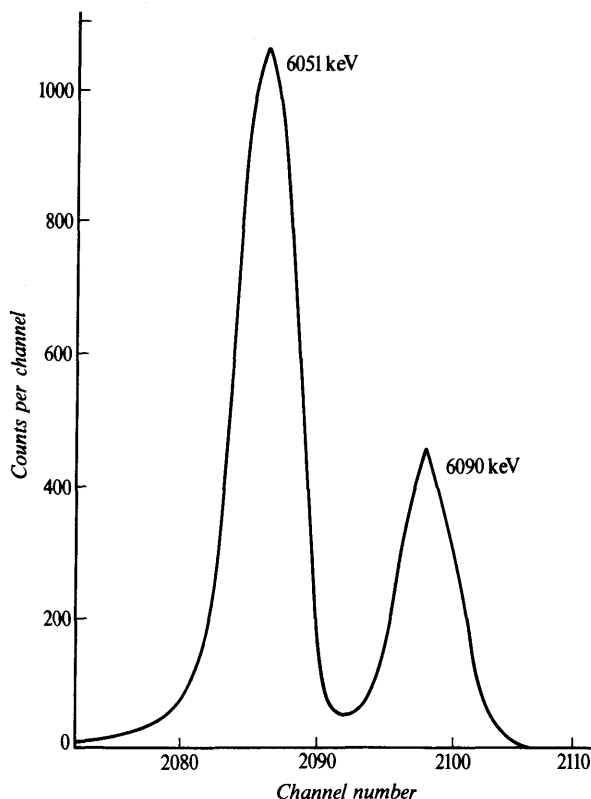


Fig. 4.18 Semiconductor counter: pulse-height distribution for 6-MeV  $\alpha$ -particles from  $^{212}\text{Bi}$  (ThC) detected in a silicon surface-barrier counter 134  $\mu\text{m}$  thick. The groups are of width 16 keV at half maximum intensity (England, J. B. A.).

consequent fast response time permitting a high counting rate, and the fairly simple nature of the necessary electronic circuits. The solid-state counter is not actually a windowless counter because of the existence of *p*- or *n*-type insensitive layers of thickness 0.1–0.5  $\mu\text{m}$  in surface barrier and diffused junction detectors respectively. This is not a serious drawback although it adds to the line width and its effect is outweighed by the overall simplicity of the counters, permitting the use of multidetector arrays. The handling of data from such complex systems increasingly demands the availability of an on-line computer for storage of information and data processing. A special facility of high value in the use of solid-state detectors is the easy construction of *particle identification* telescopes based on energy-loss  $\times$  energy product signals (Sect. 3.2.5). Counters of a length of a few centimetres may also be used as *position sensitive*

indicators in the focal plane of a spectrometer, since it can be arranged that output pulse height depends on the distance of entry of the incident particle from the collecting electrode. A disadvantage of silicon detectors for use with heavy ions and fission fragments has already been mentioned (Sect. 3.2.3); not only does nuclear scattering by the silicon nuclei worsen resolution, but it actually gives rise to an energy defect because of the occurrence of non-ionizing transitions in the solid lattice. For this reason, gas-filled detectors can give a better resolution in this application.

Increased sensitive volumes of semiconductor detectors can be obtained by compensating the acceptor centres in a *p*-type semiconductor by the controlled addition of donor impurities. The most suitable donor is lithium because this atom has a very low ionization potential in a semiconductor and also a high mobility. The lithium is 'drifted' into the bulk material from a surface layer by raising the temperature to about 420 K in the presence of an electric field. Compensated depths of about 15 mm and active volumes (in germanium) up to 100 cm<sup>3</sup> can be made. Large-volume detectors may also be prepared from highly purified germanium (impurity concentration about 1 part in 10<sup>13</sup>). The Ge(Li) detectors must be kept at a temperature below 150 K to prevent the lithium drifting away from the counting region.

Solid-state particle detectors may show channelling effects (Sect. 3.2.4) and these must be avoided by suitable orientation of the crystal.

(ii) *Gamma-ray detectors.* The major application of the lithium-drift technique is to the germanium counter (GeLi), which has transformed the subject of gamma-ray spectroscopy. Germanium has a band gap of only 0.67 eV and must be cooled to liquid nitrogen temperature when used as a counter in order to minimize thermal excitation of electrons to the conduction band. This is an inconvenience which results in a preference for silicon counters (although these are also improved by cooling) for charged-particle spectrometry. For gamma-ray detection, however, the higher atomic number of germanium ( $Z_{\text{Ge}} = 32$ ,  $Z_{\text{Si}} = 14$ ) leads to a marked improvement in efficiency as may be seen from the expressions for the basic processes of photoelectric, Compton, and pair-production absorption given in Chapter 3. The difference between Ge(Li) and Si(Li) counters is especially marked in the energy ranges in which the photoeffect and pair production predominate because of the particular *Z*-dependence. The Ge(Li) detector cannot yet be made as large as a sodium iodide scintillator and is less suitable than the latter when the highest detection efficiency is required, but its resolution is better by more than an order of magnitude, and line widths of less than 1 keV have been reported. These are narrower than those observed for charged particles because there is no

counter 'window' and energy loss in atomic collisions is not important.

Figure 4.19 shows a spectrum of  $^{24}\text{Na}$   $\gamma$ -rays taken with a Ge(Li) detector compared with one obtained with a scintillation counter. Low-energy radiations, e.g. electrons of  $\approx 10$  keV or characteristic X-rays, may be recorded with high resolution by Si(Li) counters.

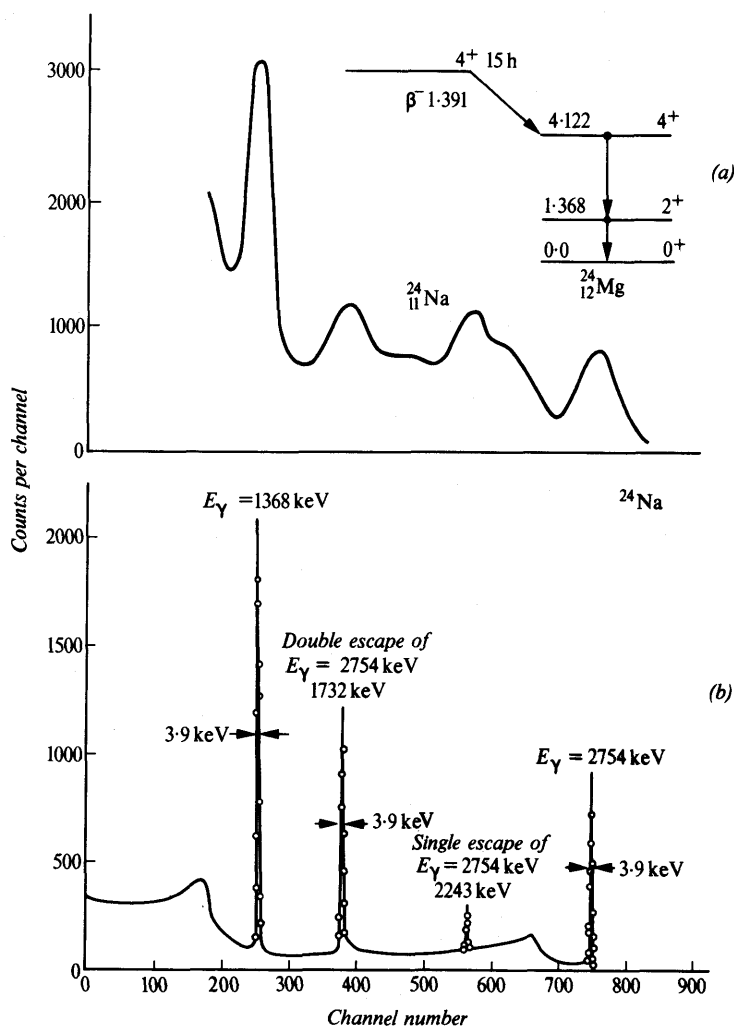


Fig. 4.19 Semiconductor counter: spectrum of radiations from  $^{24}\text{Na}$  as seen in (a) a 25 mm  $\times$  40 mm NaI(Tl) crystal, and (b) in a 30-cm<sup>3</sup> Ge(Li) detector (adapted from Orphan, V. J. and Rasmussen, N. C., *Nucl. Instrum. Meth.*, **48**, 282, 1967).



## 4.5.3 Bubble chambers (Ref. 4.5)

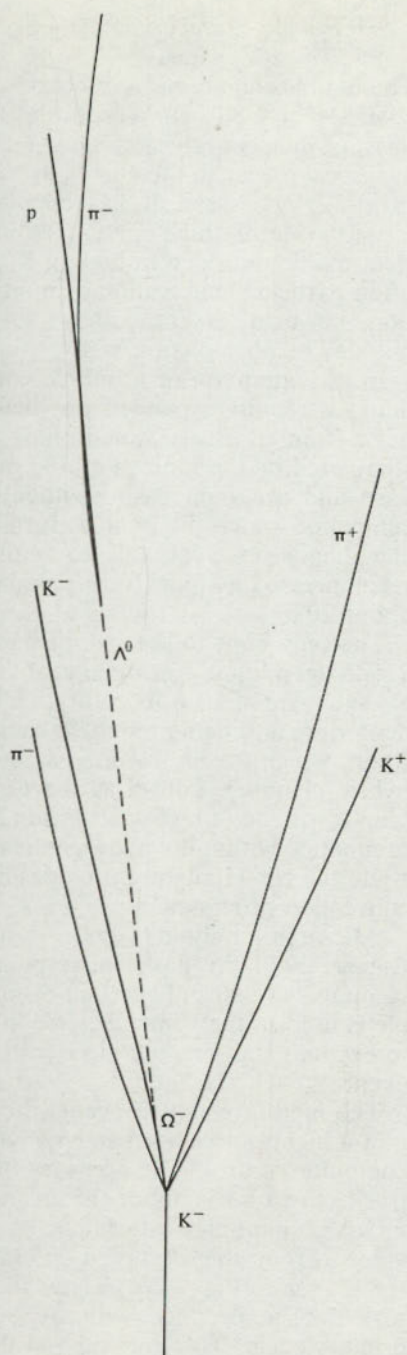
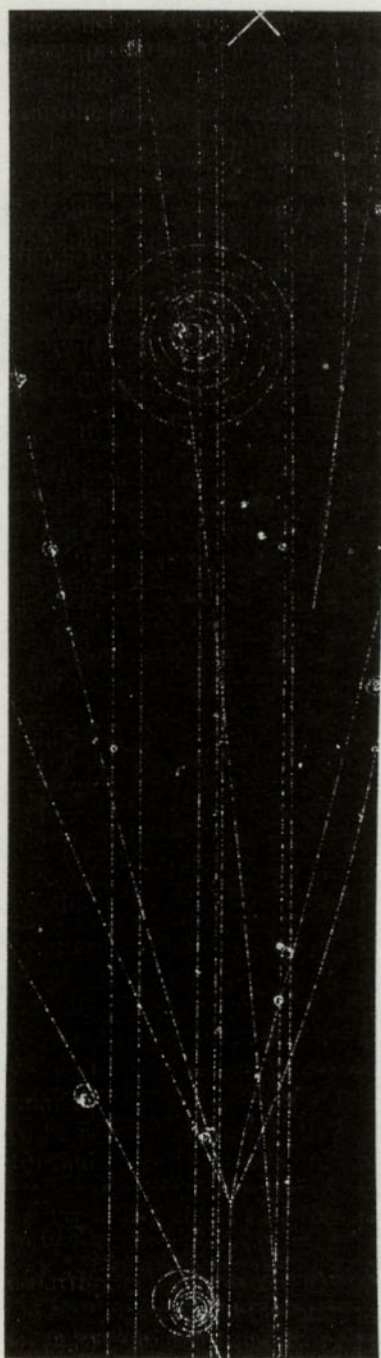
The bubble chamber is a direct descendant of the original expansion chamber of C. T. R. Wilson and like that instrument in the early days of nuclear physics, now lends aesthetic quality as well as analytical power to the events that it depicts. Following its invention in 1952 by Glaser, it has become a major detector in particle physics, offering high spatial resolution, large solid angle of detection, momentum determination if operated in a magnetic field, and often particle identification by bubble or gap density. Its time resolution, however, is not better than about 1 ms. An example of a bubble chamber picture is given in Fig. 4.20.

In the operation of a bubble chamber, a volume of superheated liquid is rapidly expanded just before the entry of a particle beam pulse from an accelerator. Boiling takes place along particle tracks, stimulated by the ionization, the bubbles reach visible size in about 1 ms and are then flash-photographed. By this time the original centres on which the bubbles formed have disappeared (so that the chamber is not adaptable to counter control) and the chamber is recompressed as quickly as possible, a complete cycle taking only about 20 ms.

The only limit to the size of bubble chambers is their cost and a 2.5-m deep liquid hydrogen chamber 3.75 m in diameter is working at the Argonne Laboratory, USA. In addition to hydrogen, deuterium and helium, bubble chamber liquids include propane and freon, which are useful for gamma-ray and neutrino detection. A hybrid chamber, known as the *track-sensitive target chamber*, contains a volume of hydrogen within a neon-hydrogen mixture. Events originating within the hydrogen may be identified without ambiguity while the Ne-H mixture provides higher density for electromagnetic conversion processes.

Although a bubble chamber cannot be triggered, it is possible to trigger the light flash in response to a signal from associated counters, so that only certain events are photographed. This principle is used in the *vertex detector* in which the role of the chamber is to examine the interaction vertex corresponding to selected types of event.

The measurement of events recorded on bubble chamber film is now a highly specialized activity based on automatic machines under computer control. The accuracy of momentum determination from track curvature is about 0.5 per cent. For particles of momentum 5 GeV/c, multiple-scattering errors in liquid hydrogen exceed this value. From the observed momentum and angles of all visible tracks, e.g. in Fig. 4.20, energy and momentum conservation can be tested in accordance with hypotheses about the nature of the primary event. This may suggest the emission of neutral particles in



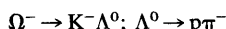
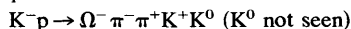
the interaction. The mass spectrum for particular groups of particles may demonstrate the formation of resonant states.

#### 4.5.4 Electronic instruments for particle physics

The bubble chamber offers excellent spatial resolution and very full information on multiparticle events, but its time resolution is poor, and, moreover, not more than about 10 charged particles per accelerator pulse can usually be handled. Electronic detectors, though offering less complete spatial information (except with great complexity), can provide a much greater data-taking capacity, approaching perhaps  $10^6$  particles per second, together with some positional and ionization density information. The advantages of visual and electronic detectors are combined in the *spark chamber* (Ref. 4.5), in which a counter signal triggers the application of a high-voltage pulse in about  $1\text{ }\mu\text{s}$  to a bank of thin plates between which discharges then take place near the particle tracks. The pulse can be applied before the primary centres disappear, so that counter control is possible, in contrast with the bubble chamber. Readout from triggered chambers, which usually operate in a magnetic field, may be visual (on film), visual (using a TV camera), acoustic (using transducers) or electrical (using wires to fill chamber planes). Spark chambers have dead times of about 10 ms and may be triggered perhaps 20 times during an accelerator beam pulse.

A popular instrument of high data-gathering power is the *multi-wire proportional counter* (MWPC), which is an array of anode wires  $20\text{ }\mu\text{m}$  in diameter with 1–2 mm spacing placed between high-voltage conducting cathode planes in a gas at low pressure. The operation of an individual wire/plane is exactly as for a simple proportional counter (Ref. 4.4) and offers a time resolution of 20 ns with a dead time of less than  $1\text{ }\mu\text{s}$ , compared with perhaps 10 ms for the much heavier discharge used in the spark chamber. Such chambers are operated continuously but the signals are small and amplification is required for each individual wire. In the *drift chamber*, additional spatial resolution is obtained by measuring the time that electrons from the particle track and subsequent multiplication take to travel to the nearest positively charged wire. The cathode planes are replaced by negative wires, and the total number of wires can be reduced with respect to the MWPC and higher positional accuracy obtained.

Fig. 4.20 Bubble chamber picture of the production and decay of the strange baryon  $\Omega^-$  in the kaon-proton reaction



(Birmingham University Bubble Chamber Group.)

Electronic methods of velocity ( $\beta$ ) measurement based on the Cherenkov effect have already been mentioned (Sect. 3.1.3). For a particle of known momentum  $p$ , these immediately give mass information, since (with  $c = 1$ )  $p = \beta\gamma M = \beta M/(1 - \beta^2)^{1/2}$ . Simpler still is the time-of-flight method using fast counters that is widely used for neutron energy measurement in all ranges of velocity.

## 4.6 Summary

This chapter surveys some of the developments in nuclear technology that have taken place since 1930. Accelerators for charged particles have developed from the voltage-multiplier of Cockcroft and Walton, the drift-tube accelerator of Wideroe and the cyclotron of Lawrence to the modern alternating-gradient proton synchrotron and the electron linear accelerator, each able to feed storage-ring systems. Brief mention is made of the beam-handling equipment that conveys accelerated particles to a target, in which nuclear transmutations, including elementary particle reactions, may take place. The study of these events requires a detector system that is matched to the performance of the accelerator with which it is to be used. The main features of a simple magnetic spectrometer, and of scintillation and solid-state particle and photon counters are described. The significance of track chambers and proportional counters for particle physics is noted.

## Examples 4

- 4.1 Calculate the velocity of a proton of energy 10 MeV as a fraction of the velocity of light. [0.15]  
How long would a proton take to move from the ion source to the target in a uniform 10 MV accelerating tube 3 m long? [ $1.4 \times 10^{-7}$  s]
- 4.2 A belt system of total width 0.3 m charges the electrode of an electrostatic generator at a speed of  $20 \text{ m s}^{-1}$ . If the breakdown strength of the gas surrounding the belts is  $3 \text{ MV m}^{-1}$  calculate:  
(a) the maximum charging current, [320  $\mu\text{A}$ ]  
(b) the maximum rate of rise of electrode potential, assuming a capacitance of 111 pF and no load current. [ $2.9 \text{ MV s}^{-1}$ ]
- 4.3 A magnetic field is being explored by the 'floating wire' method. If the current in the wire is 2 amperes and the tension is set at 0.5 kg weight, what is the energy of the proton whose trajectory is followed by the wire? [252 MeV]
- 4.4 In high-energy physics, it is customary to measure momenta in the unit MeV/c. Using the relativistic formula (4.14) find the momentum (in MeV/c) of:  
(a) a 1000-MeV proton, [1696]  
(b) a 1-MeV proton, [43.4]  
(c) a 10-MeV photon, [10]  
(d) a 100-MeV electron. [101]
- 4.5 Calculate the value of  $\beta$  ( $=v/c$ ) for protons of the following energies: 100 MeV, 500 MeV, 1000 MeV. [0.43, 0.76, 0.87]
- 4.6 The peak potential difference between the dees of a cyclotron is 25 000 V and the magnetic field is 1.6 T. If the maximum radius is 0.3 m, find the energy

acquired by a proton in electron volts and the number of revolutions in its path to the extreme radius. [11.0 MeV, 220]

- 4.7** Deuterons of energy 15 MeV are extracted from a cyclotron at a radius of 0.51 m by applying an electric field of  $6 \text{ MV m}^{-1}$  over an orbit arc of  $90^\circ$ . Calculate the equivalent reduction of magnetic field and the resulting increase in orbit radius  $\Delta r$ . [0.16 T, 0.053 m]
- 4.8** Calculate the cyclotron frequency for non-relativistic deuterons in a field of 1 T. [7.6 MHz]
- 4.9** A pulse of  $10^{10}$  particles of single charge is injected into a cyclic accelerator and is kept circulating in a stable orbit by the application of a radiofrequency field. What is the mean current when the radiofrequency is 7 MHz? [11.2 mA]
- 4.10** Calculate the energy between the photopeak and the high-energy edge of the Compton electron distribution in the pulse-height spectrum from a scintillator detecting  $\gamma$ -radiation of energy  $m_e c^2$ . What would the energy of the back-scattered peak be? [170 keV]
- 4.11** Verify that the ratio of peak heights in Fig. 4.16c is reasonable, using the mass attenuation coefficients given in Reference 2.1, Fig. 1.6, p. 717.
- 4.12** In the time-of-flight method for determining particle energies (Sect. 4.1) particles of rest energy  $E_0$  and kinetic energy  $T$  are observed over a flight path  $L$ . Show that the time of flight is  $t = L/c \cdot (1 - E_0^2/(E_0 + T)^2)^{-1/2}$ .
- 4.13\*** A heavy ion of mass number  $A_1$  bombards a target atom of mass number  $A_2$ . If each nucleus behaves as a sphere of charge of radius  $r_0 A^{1/3}$  ( $r_0 = 1.2 \text{ fm}$ ) show that the Coulomb potential barrier is

$$V_C = \frac{(A_1 + A_2)Z_1 Z_2 e^2}{4\pi\epsilon_0 A_2 r_0 (A_1^{1/3} + A_2^{1/3})}$$

where  $Z_1, Z_2$  are the atomic numbers. Evaluate this for  $A_1 = A_2 = 125$ ,  $Z_1 = Z_2 = 52$ . [648 MeV]

- 4.14\*** In the Stanford linear accelerator, electrons reach an energy of 20 GeV in a distance of 3 km. Assuming that increments of energy are uniform and that the injection energy is 10 MeV, find the effective length of the accelerator to an electron.
- 4.15\*** Taking the magnetic potential in a quadrupole field to be  $V = Gxy$ , deduce the  $x, y$  components of the force on a charged particle moving with uniform velocity  $v$  along the  $z$ -axis and show that they are proportional (a) to the field gradient, and (b) to the component displacement.

